Oxygen diffusion in hcp metals from first principles

Henry H. Wu,[1,2] Pandu Wisesa,[1,3] and Dallas R. Trinkle[1,*]

[1]*Department of Materials Science and Engineering, University of Illinois, Urbana-Champaign, Illinois 61801, USA*

[2]*Department of Materials Science and Engineering, University of Wisconsin, Madison, Wisconsin 53706, USA*

[3]*Department of Materials Science and Engineering, Johns Hopkins University, Baltimore, Maryland 21218, USA*

(Received 20 May 2016; published 15 July 2016)

Oxygen interstitial site energies and migration barriers in 15 hexagonal close-packed (hcp) metals have been calculated with first-principles density functional theory. Multiple hcp systems show a preference for the hexahedral site over the tetrahedral site, as well as a stable crowdion site. More surprisingly, in more than half of the hcp systems, the oxygen does not choose the large octahedral interstitial as its ground state. We explain this result based on the effective valence of the metal from crystal-field splitting and the c/a ratio. Diffusion constants for oxygen in all 15 hcp systems are calculated from analytically derived diffusion equations and match available experimental data.

DOI: 10.1103/PhysRevB.94.014307

I. INTRODUCTION

The presence of light element impurities determine many materials properties in metals, including phase transition kinetics [1], precipitates in semiconductors [2], and hydrogen embrittlement in steels [3]. Oxygen content in particular need to be carefully controlled to balance the increase in hardness with decrease in ductility [4]. While many studies have experimentally measured [5–20] or computationally predicted [21–24] the diffusion of oxygen through various metal alloy systems, there is a lack of a fundamental atomistic understanding of how oxygen diffuses through many basic metal systems in a systematic manner.

The hexagonal close-packed (hcp) crystal structure is space group [25] 194, $P6_3/mmc$, and is the low-temperature phase for many elements. Even in this simple lattice it is difficult to experimentally determine the atomistic mechanisms for interstitial diffusion. Contributing to this difficulty is the short residence time of the interstitial species at metastable configurations. However, even the exact ground-state configuration can be hard to confirm since low interstitial solubility limits the use of x-ray diffraction.

We conduct a systematic first-principles study of various oxygen interstitial sites and diffusion pathways through all 15 hcp elements (not including the lanthanides): Be, Cd, Co, Hf, Mg, Os, Re, Ru, Sc, Tc, Ti, Tl, Y, Zn, and Zr. We find a variety of metastable configurations for the oxygen interstitial which results in four diffusion networks for oxygen in these 15 hcp metals. The relative stability of octahedral or tetrahedral sites in different metals is understood based on the effective valence from crystal-field splitting and the c/a ratio. We derive analytic diffusion equations for each of the four networks and find good agreement with available experimental oxygen diffusion data. This work showcases the variety of diffusion behavior for oxygen in hcp metals.

II. COMPUTATIONAL DETAILS

First-principles calculations are performed with VASP [26–29], a plane-wave density-functional theory (DFT) code. Oxygen and each of the 15 hcp elements are treated with projector augmented-wave (PAW) method [30] with the PBE generalized gradient approximation [31]. Table I lists the valence configuration for all pseudopotentials used. To accurately describe the diffusion of oxygen in the Co system, we conduct spin-polarized calculations. We choose the PAW method in order to obtain the all-electron charge densities for analysis with improved Bader integration [32,33]. We use a single oxygen atom with 96 lattice atoms in a $4 \times 4 \times 3$ hcp supercell with $4 \times 4 \times 4$ k-point mesh. A plane-wave cutoff of 400 eV is used for all metals and is converged to 0.3 meV/atom. The k-point mesh with Methfessel-Paxton smearing of 0.2 eV is converged to 1 meV/atom. To determine energy barriers for interstitial hops, we use the climbing-image nudged elastic band [34,35] method with one intermediate image and constant cell shape. Since we only consider simple transitions involving only a single interstitial atom, one image is sufficient to determine the transition saddle point. With the climbing-image modification, the force on the image along the path is negated, while components perpendicular to the path are unchanged; the image relaxed to an extremum where the forces are less than 5 meV/Å, and restoring forces confirm that this extremum is a first-order saddle point.

III. RESULTS AND DISCUSSION

Figure 1 shows the location for various observed oxygen interstitial defects in the hcp lattice as well as their Wyckoff positions [25]. For hcp systems, the most commonly discussed interstitials are the octahedral and tetrahedral, with six and four equivalent neighboring atoms, respectively. Recently, it has been found through DFT calculations that oxygen in titanium occupies the hexahedral site [1] rather than tetrahedral and oxygen is also metastable at the nonbasal crowdion site in titanium [21]. The hexahedral site is fivefold coordinated with three nearest lattice atom neighbors in the basal plane and two further neighbors directly above and below. The nonbasal crowdion site is sixfold coordinated with two significantly displaced lattice atom neighbors and four further neighbors. While all hcp systems contain a (meta)stable octahedral site, the other interstitial sites are not stable in all systems. Indeed, the tetrahedral and hexahedral sites are mutually exclusive

*dtrinkle@illinois.edu

TABLE I. PAW pseudopotential valence configurations for the 15 hcp elements and oxygen.

	Valence configurations		
O	$2s^2 2p^4$	Ru	$4d^7 5s^1$
Be	$2s^2$	Sc	$3s^2 3p^6 3d^2 4s^1$
Cd	$4d^{10} 5s^2$	Tc	$4p^6 4d^5 5s^2$
Co	$3d^7 4s^2$	Ti	$3p^6 3d^2 4s^2$
Hf	$5p^6 5d^2 6s^2$	Tl	$5d^{10} 6s^2 6p^1$
Mg	$3s^2$	Y	$4s^2 4p^6 4d^1 5s^2$
Os	$5d^6 6s^2$	Zn	$3d^{10} 4s^2$
Re	$5d^5 6s^2$	Zr	$4s^2 4p^6 4d^3 5s^1$

for all 15 systems studied. It should also be mentioned that for all systems with stable tetrahedral sites, the oxygen does not reside at the perfect tetrahedral positions as shown in Fig. 1. Rather, oxygen displaces away from the basal face of the tetrahedral site for Os, Re, Ru, and Tc, and displaces towards the basal face for the remaining tetrahedral systems. Other high-symmetry sites, such as the basal crowdion, were not found to be metastable for oxygen in any of the 15 hcp elements studied.

Figure 2 shows all possible transitions between interstitial sites in hcp systems. Since tetrahedral and hexahedral sites do not coexist in any system, no H-T transition networks are shown. For networks which contain the tetrahedral site, the T-T transition is also included in the figure. The T-T transition is a local jump between neighboring tetrahedral sites and allows c-axis mobility in those single networks. Depending on the available interstitials for each system, octahedral sites may be connected to six distinct tetrahedral sites, six hexahedral sites, six crowdion sites, and two other octahedrals. Tetrahedral sites connect to three octahedral sites, three crowdion sites, and

Site	Wyckoff pos.	Site	Wyckoff pos.
octahedral	$2a$ $(0,0,0)$	hexahedral	$2d$ $(\frac{2}{3},\frac{1}{3},\frac{1}{4})$
tetrahedral	$4f$ $(\frac{2}{3},\frac{1}{3},\frac{1}{8})$	crowdion	$6g$ $(\frac{1}{2},0,0)$

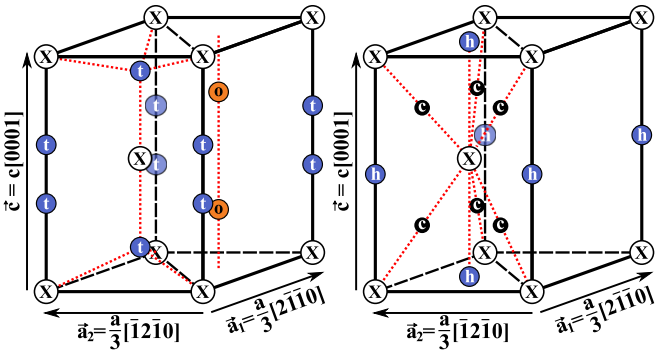

FIG. 1. Wyckoff positions and unit-cell locations for oxygen interstitial sites in hcp systems. On the left: **o**ctahedral (orange) and **t**etrahedral (blue). On the right: **h**exahedral (blue) and **c**rowdion (black).

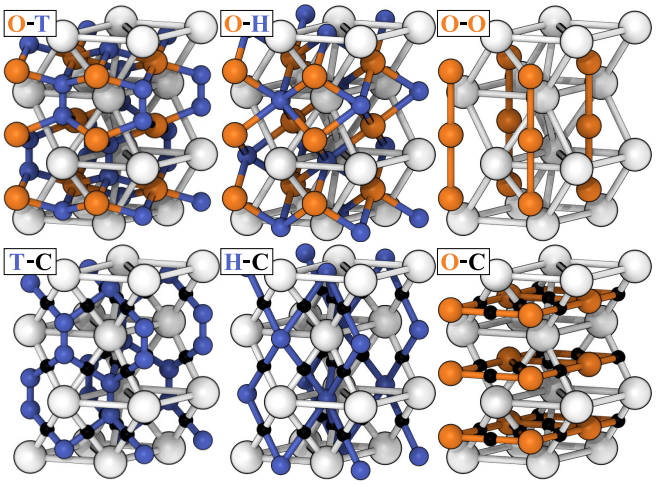

FIG. 2. Connectivity network for transitions between interstitial sites in the hcp lattice. Note that the O-T and T-C networks also include T-T transitions between neighboring tetrahedral sites. White spheres represent the hcp lattice atoms, orange for octahedral, blue for tetrahedral and hexahedral, and black for crowdion interstitial sites.

the neighboring tetrahedral site. Hexahedral sites connect to six octahedral sites and six crowdion sites. Crowdion sites connect to two octahedral sites, two tetrahedral sites, and two hexahedral sites. The complete oxygen diffusion network for each specific hcp system is the summation of all the networks in Fig. 2 which contain interstitial sites available to that system.

The analytic diffusion equations for each of the individual diffusion networks (Fig. 2) are given in Table II. The diffusion equations are given in terms of λ_{ij}, the transition rate for oxygen jumping from site i to site j. At temperature T, λ_{ij} is equal to the Arrhenius equation: $\lambda_{ij} = \nu_{ij} \exp(-E_{ij}/k_B T)$, where ν_{ij} is the attempt prefactor for the transition and E_{ij} is the energy barrier relative to the site energy of site i. Please note that since these equations are for the transition networks independent of one another, comparisons can only be made after applying the appropriate fractional occupancy for sites in the network.

TABLE II. Analytic diffusion equations for individual transition networks from Fig. 2.

	$a^{-2} D_{\text{basal}}$	$c^{-2} D_{\text{c axis}}$
O-T	$\dfrac{\lambda_{\text{ot}}\lambda_{\text{to}}}{2\lambda_{\text{ot}} + \lambda_{\text{to}}}$	$\dfrac{1}{4}\dfrac{3\lambda_{\text{ot}}\lambda_{\text{to}}\lambda_{\text{tt}}}{(2\lambda_{\text{ot}} + \lambda_{\text{to}})(3\lambda_{\text{to}} + 2\lambda_{\text{tt}})}$
O-H	$\dfrac{\lambda_{\text{oh}}\lambda_{\text{ho}}}{\lambda_{\text{oh}} + \lambda_{\text{ho}}}$	$\dfrac{1}{8}\dfrac{3\lambda_{\text{oh}}\lambda_{\text{ho}}}{\lambda_{\text{oh}} + \lambda_{\text{ho}}}$
O-O	0	$\dfrac{1}{4}\lambda_{\text{oo}}$
T-C	$\dfrac{1}{4}\dfrac{\lambda_{\text{tc}}\lambda_{\text{ct}}}{3\lambda_{\text{tc}} + 2\lambda_{\text{ct}}}$	$\dfrac{1}{4}\dfrac{3\lambda_{\text{tc}}\lambda_{\text{ct}}\lambda_{\text{tt}}}{(3\lambda_{\text{tc}} + 2\lambda_{\text{ct}})(3\lambda_{\text{tc}} + 2\lambda_{\text{tt}})}$
H-C	$\dfrac{1}{4}\dfrac{\lambda_{\text{hc}}\lambda_{\text{ch}}}{3\lambda_{\text{hc}} + \lambda_{\text{ch}}}$	$\dfrac{1}{8}\dfrac{3\lambda_{\text{hc}}\lambda_{\text{ch}}}{3\lambda_{\text{hc}} + \lambda_{\text{ch}}}$
O-C	$\dfrac{1}{4}\dfrac{3\lambda_{\text{oc}}\lambda_{\text{co}}}{3\lambda_{\text{oc}} + \lambda_{\text{co}}}$	0

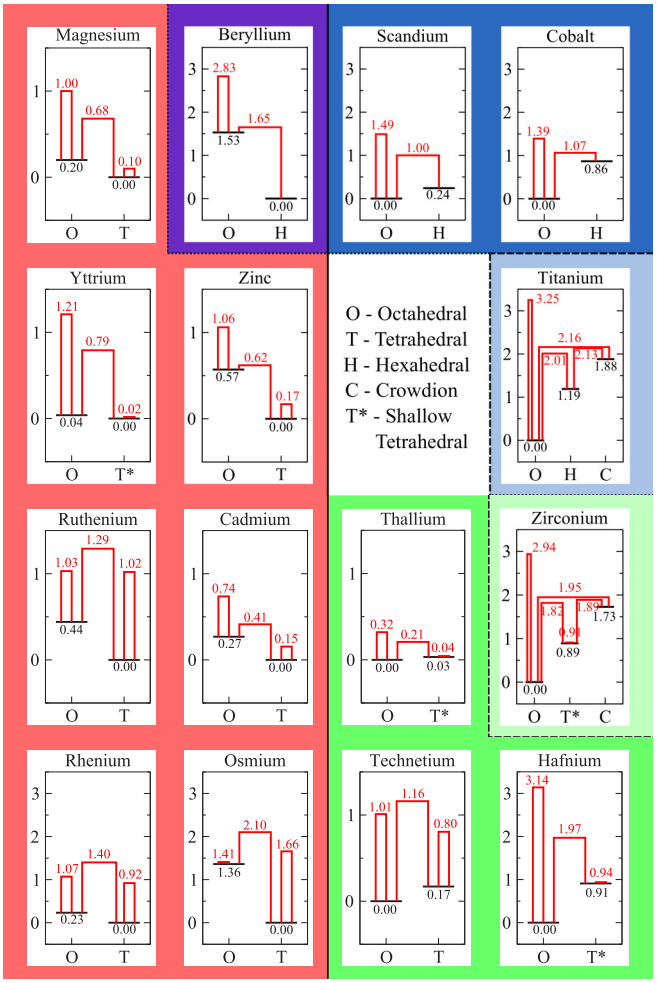

FIG. 3. Oxygen interstitial site energies and diffusion barriers in all 15 hcp elements. Energy in units of eV is represented on the vertical axis, while possible metastable interstitial sites for each element are placed on the horizontal axis. The elements are grouped by commonalities of interstitial stability; on the right, elements have the octahedral interstitial site as the ground-state configuration, while elements on the left do not. The dotted line separates elements with hexahedral sites (Be, Co, Sc, and Ti) versus elements with tetrahedral sites. The dashed line separates elements with crowdion sites (Ti and Zr) versus elements that do not. Relative site energies are given in black, while possible transitions between sites are connected by red lines with the respective saddle point energies given in red, also relative to the ground-state configuration energy. Some tetrahedral sites are labeled shallow tetrahedral (T*) due to the low T-T transition barrier in that element.

Figure 3 shows the relative DFT site energies and diffusion barriers for oxygen in all 15 studied hcp systems. Site energies are listed relative to the lowest-energy interstitial configuration in each hcp system. As an example, the Ti diagram in the upper right of the figure shows three interstitial sites for oxygen in titanium (O[+0.00 eV], H[+1.19 eV], C[+1.88 eV]). One surprising result is that the octahedral site, with the largest interstitial volume, is not always the ground-state configuration. Indeed, the octahedral site is the ground state for oxygen in only seven of the hcp systems (Co, Hf, Sc, Tc, Ti, Tl, and Zr); oxygen prefers to reside in the tetrahedral or hexahedral in the remaining eight systems. Oxygen in hcp overwhelmingly prefer the tetrahedral site over the hexahedral site; only Be, Co, Sc, and Ti contain the hexahedral site. The crowdion site is even more rare, as it is only metastable in Ti and Zr.

Transitions between sites are shown in Fig. 3 by red lines connecting the sites, with the transition saddle-point energies listed in red along the connecting lines. As an example, the Ti diagram in the upper right of the figure shows four possible transitions: O-O with a saddle-point energy of 3.25 eV, 2.10 eV for O-H, 2.13 eV for H-C, and 2.16 eV for O-C. Please note that the values given for the saddle-point energies are also relative to the ground-state configuration energy for each system. Red lines which begin and end on the same site represent a transition to a neighboring site of the same type (O-O, T-T). Refer to Fig. 2 to visualize how the different transitions appear in the hcp lattice. Tetrahedral sites for Hf, Tl, Y, and Zr are labeled as T* and are referred to as shallow tetrahedrals due to the very low T-T barrier (< 0.03 eV) connecting neighboring tetrahedral sites. This shallow barrier may allow the formation of a pseudohexahedral configuration at high temperatures.

Few first-principles calculations for oxygen in hcp are available in the literature. One comparison has been done by Middleburgh and Grimes [22], where they used DFT to study various defects and their diffusion in beryllium. They found that oxygen relaxes to the hexahedral site from the tetrahedral and that the octahedral site is 1.38 eV higher in energy than the hexahedral (our calculations give 1.53 eV higher). They also found the O-O barrier to be 2.71 eV and the O-H barrier to be 1.63 eV, both energies are relative to the hexahedral site energy. Our calculations give 2.83 eV for the O-O barrier and 1.65 eV for the O-H barrier, again relative to the hexahedral site energy. Another DFT study done by Zhang *et al.* [23] gives very similar results, with the octahedral being 1.50 eV higher than hexahedral, O-O barrier to be 2.76 eV, and O-H barrier at 1.63 eV. The excellent agreement with two separate DFT calculations for oxygen diffusion in beryllium serves as validation of our methodology for the other hcp systems.

Following our previous work [21,36,37], we have derived full analytic diffusion equations for oxygen in each hcp system. For different hcp systems, the diffusion equations in the basal and c-axis directions are distinct according to the set of interstitial sites possible ({O, T}, {O, H}, {O, T, C}, {O, H, C}). For systems with only octahedral and tetrahedral sites (Cd, Hf, Mg, Os, Re, Ru, Tc, Tl, Y, and Zn),

$$D_{\text{basal}} = a^2\left[\frac{\lambda_{\text{ot}}\lambda_{\text{to}}}{2\lambda_{\text{ot}}+\lambda_{\text{to}}}\right],$$
$$D_c = \frac{1}{4}c^2\left[\frac{\lambda_{\text{ot}}(3\lambda_{\text{to}}\lambda_{\text{tt}}+3\lambda_{\text{oo}}\lambda_{\text{to}}+2\lambda_{\text{oo}}\lambda_{\text{tt}})}{(2\lambda_{\text{ot}}+\lambda_{\text{to}})(3\lambda_{\text{to}}+2\lambda_{\text{tt}})}\right]. \quad (1)$$

For systems with only octahedral and hexahedral sites (Be, Co, and Sc),

$$D_{\text{basal}} = a^2\left[\frac{\lambda_{\text{oh}}\lambda_{\text{ho}}}{\lambda_{\text{oh}}+\lambda_{\text{ho}}}\right],$$
$$D_c = \frac{1}{8}c^2\left[\frac{\lambda_{\text{oh}}(3\lambda_{\text{ho}}+2\lambda_{\text{oo}})}{\lambda_{\text{oh}}+\lambda_{\text{ho}}}\right]. \quad (2)$$

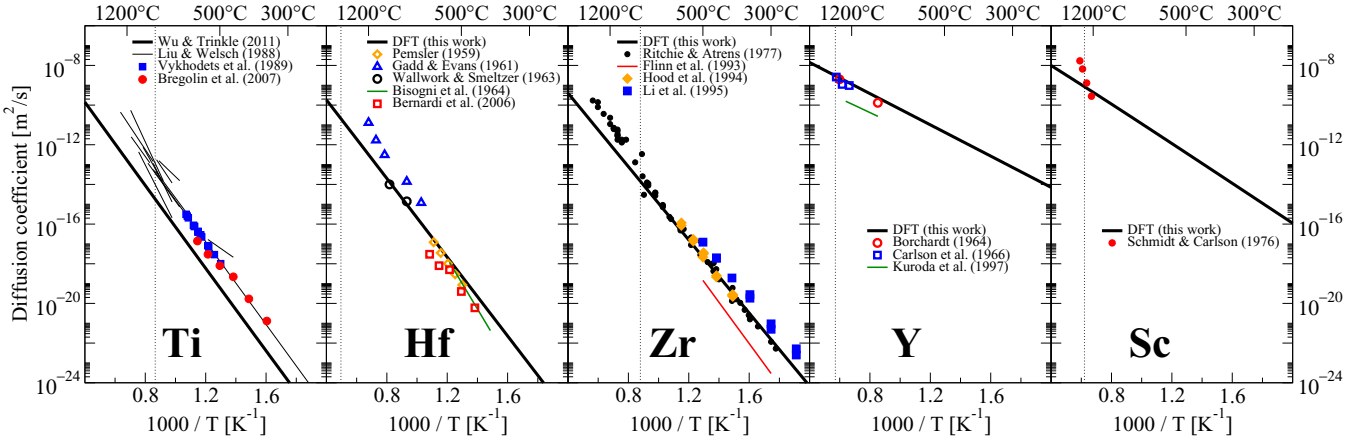

FIG. 4. Comparison between our DFT predicted and experimentally measured oxygen diffusivity in Ti [5–7], Hf [8–12], Zr [13–16], Y [17–19], and Sc [20]. We have previously reported the DFT data for oxygen diffusion in titanium [21], while the other DFT predictions are from this work. For Ti, the data labeled as Liu and Welsch come from their review paper covering experiments ranging from 1957–1983. For Zr, the data labeled as Ritchie and Atrens come from their review paper, the data points plotted only include experiments without the effect of grain boundary diffusion. The vertical dotted lines show the α-β transition temperatures for each element: 1155 K for Ti, 2016 K for Hf, 1137 K for Zr, 1751 K for Y, and 1610 K for Sc.

Only Zr contains octahedral, tetrahedral, and crowdion sites, the simplified equations are

$$D_{\text{basal}} = a_{\text{Zr}}^2\left[\ \lambda_{\text{ot}} + \frac{3}{4}\lambda_{\text{oc}} + \ \frac{1}{8}\lambda_{\text{tc}}\left(\frac{\lambda_{\text{ot}}}{\lambda_{\text{to}}}\right) + 0\lambda_{\text{oo}}\right],$$
$$D_c = c_{\text{Zr}}^2\left[\frac{3}{8}\lambda_{\text{ot}} + 0\lambda_{\text{oc}} + \frac{3}{16}\lambda_{\text{tc}}\left(\frac{\lambda_{\text{ot}}}{\lambda_{\text{to}}}\right) + \frac{1}{4}\lambda_{\text{oo}}\right]. \quad (3)$$

Only Ti contains octahedral, hexahedral, and crowdion sites; the simplified equations are

$$D_{\text{basal}} = a_{\text{Ti}}^2\left[\ \lambda_{\text{oh}} + \frac{3}{4}\lambda_{\text{oc}} + \frac{1}{4}\lambda_{\text{hc}}\left(\frac{\lambda_{\text{oh}}}{\lambda_{\text{ho}}}\right) + 0\lambda_{\text{oo}}\right],$$
$$D_c = c_{\text{Ti}}^2\left[\frac{3}{8}\lambda_{\text{oh}} + 0\lambda_{\text{oc}} + \frac{3}{8}\lambda_{\text{hc}}\left(\frac{\lambda_{\text{oh}}}{\lambda_{\text{ho}}}\right) + \frac{1}{4}\lambda_{\text{oo}}\right]. \quad (4)$$

The simplified equations for Zr and Ti are derived from the general diffusion equations for O-T-C and O-H-C transition networks. The simplification process assumes, relative to k_BT, that the octahedral site is much lower in energy than tetrahedral and hexahedral sites, which are in turn much lower in energy than crowdion sites; and that the T-T transition barrier is also much lower in energy than k_BT. These assumptions are justified for the cases of oxygen diffusion in Zr and Ti, and the diffusion equations simplify into the sum of diffusion equations for individual diffusion networks (Fig. 2, Table II). From left to right, the terms in the Zr diffusion equations [Eq. (3)] represent contribution from O-T, O-C, T-C, and O-O. From left to right, the terms in the Ti diffusion equations (4) represent contribution from O-H, O-C, H-C, and O-O.

To obtain the DFT diffusion plots shown in Figs. 4 and 5, we compute transitions rates λ_{ij} for each element according to the corresponding Eqs. (1)–(4). While we have the DFT energy barriers E_{ij} from Fig. 3, we still require the attempt frequencies ν_{ij}. For the case of oxygen in titanium [21], this was done by calculating the Vineyard attempt frequency [41] for each individual transition. In this work, we approximate all the attempt frequencies for oxygen in a single hcp system as ν, calculated from

$$\frac{\nu}{\nu_{\text{D}}} = \sqrt{\frac{m_{\text{matrix}}}{m_{\text{oxygen}}}}, \quad (5)$$

where m_{matrix} is the mass of the hcp matrix atom, m_{oxygen} is the mass of oxygen, and ν_{D} is the Debye frequency for each hcp element. The Debye frequency ν_{D} is computed from the element's Debye temperature [38–40] (T_{D}) with the relation $T_{\text{D}} = \nu_{\text{D}}(h/k_B)$. This approximation is reasonable because the lattice vibration frequency is generally the same order of magnitude as the diffusion attempt frequency, which should scale with the mass ratios of the diffusant and matrix. For Ti, $T_{\text{D}} = 425$ K ($\nu_{\text{D}} = 8.85$ THz), giving an attempt frequency of

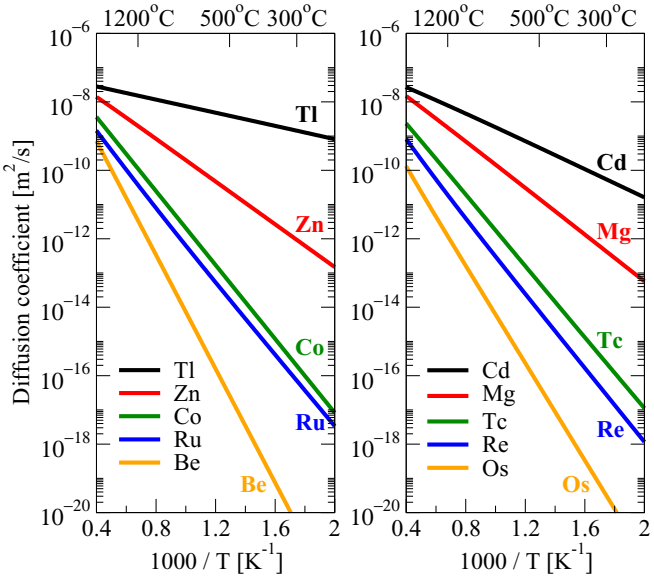

FIG. 5. DFT oxygen diffusion predictions for the remaining 10 hcp elements. No experimental data were found in the literature.

TABLE III. Debye temperature [38–40] (T_D), Debye frequency (ν_D), and attempt frequency ($\nu = \nu_D(m_{matrix}/m_{oxygen})^{1/2}$) for hcp elements, not including Ti. ν_D is used to approximate the attempt frequency in diffusion calculations.

	Be	Cd	Co	Hf	Mg	Os	Re
T_D (K)	1463	214	453	251	387	477	405
ν_D (THz)	30.48	4.45	9.44	5.23	8.05	9.94	8.44
ν (THz)	22.88	11.81	18.12	17.47	9.92	34.27	28.79
	Ru	Sc	Tc	Tl	Y	Zn	Zr
T_D (K)	499	362	454	79	257	327	296
ν_D (THz)	10.40	7.55	9.46	1.65	5.35	6.81	6.16
ν (THz)	26.14	12.65	23.41	5.90	12.62	13.77	14.72

$\nu = 15.31$ THz. This value is comparable to the previously reported DFT attempt frequencies, all of which, with one exception, were above 10 THz. The Debye temperatures, Debye frequencies, and the approximate attempt frequencies for the 14 hcp elements (excluding Ti) are listed in Table III.

Figure 4 shows comparisons between oxygen diffusion coefficients calculated from DFT and experimentally reported diffusion data for Ti, Hf, Zr, Y, and Sc. Oxygen diffusion in Ti, Hf, and Zr make up the vast majority of available experimental literature, with fewer reports found for Y and Sc. The overall diffusion energy slope for Ti, Hf, Zr, and Y match very well between the DFT diffusion curves and the experimental data. The absolute DFT diffusivity values for these Hf, Zr, and Y also lie within the experimental spread while Ti shows an underestimation of the diffusion prefactor [21]. Our predicted slope for oxygen diffusion in scandium disagrees significantly with the single experiment available [20]. The DFT diffusion barriers that we calculated for scandium are not substantially different when compared to those of the other 14 hcp elements, and no indication from the calculations that there are different mechanisms at work for oxygen in scandium. It is possible that the discrepancy is due to the experiment's attempt to measure the diffusivity near the α-β transition temperature for Sc. Figure 5 shows the predicted DFT oxygen diffusivity curves for the remaining 10 hcp elements. We were not able to find any experimental results in the literature for oxygen diffusion in these elements.

Figure 6 plots various system properties of the hcp elements against the relative stability of the oxygen interstitial sites. Figure 6(a) shows a comparison between the hcp lattice parameter and c/a ratio. In Figs. 6(b) and 6(c), the numerical energy difference between oxygen at the octahedral site versus the tetrahedral/hexahedral site is compared to the common metal valence and the first ionization energy, respectively. A lower ionization energy is weakly correlated to increased octahedral stability, while a V-shaped trend exists between the valence and octahedral stability. A different way to group the metal valence is through crystal-field theory. For hexagonal configuration, the crystal-field splitting for the d orbital has d_{z^2} at the lowest energy, above which are the degenerate d_{xy} and d_{yz}, above that is $d_{x^2-y^2}$, and finally d_{xy} at the highest energy level. With this splitting, the 15 hcp elements can be divided into three different groups: (1) full shells of paired d electrons, Be, Mg, Ru, Os, Zn, and Cd; (2) single unpaired

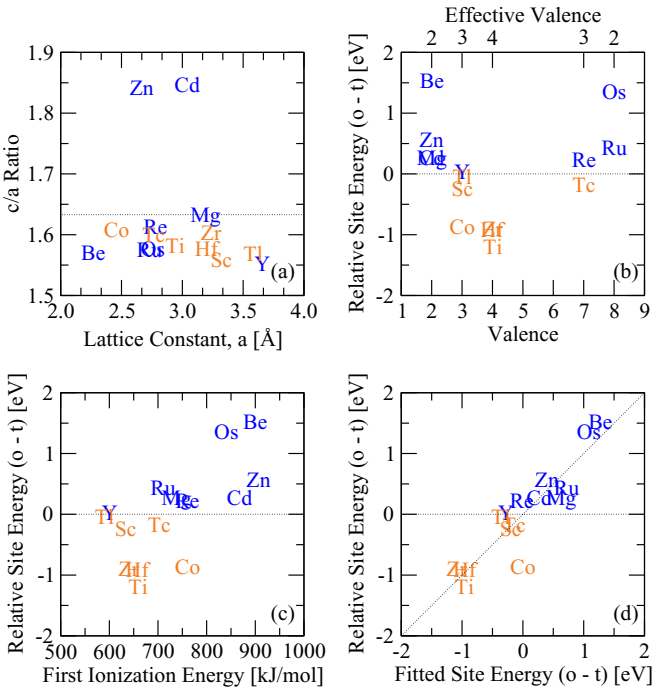

FIG. 6. Correlation between the relative oxygen interstitial site energy and physical properties of the 15 hcp elements. Each elemental symbol is centered on the corresponding data for that element. (a) Comparison of the lattice constant and the c/a ratio for the hcp elements. The dotted line represents the ideal hcp $c/a = 1.633$. (b) Correlation between the octahedral–tetrahedral/hexahedral energy difference and the common metal valence as well as the effective valence. (c) Correlation between the octahedral–tetrahedral/hexahedral energy difference and the first ionization energy. (d) Linear regression fit ($R^2 = 0.8240$) of the DFT relative site energies to the c/a ratio, the effective valence, and the first ionization energy. The primary outlier is Co, due to its magnetic ordering. The effective valence is determined according to crytal-field splitting. hcp elements are colored according to the oxygen ground-state configuration in that element, orange for octahedral site and blue for tetrahedral/hexahedral site.

electron, Sc, Y, Tc, Re, Co, and Tl (unpaired p electron); (3) two unpaired electrons (one in each of the degenerate d_{xy} and d_{yz}), Ti, Zr, and Hf. Under this grouping, Os and Ru belong with the two-valent elements, while Re and Tc belong with the three-valent elements. This effective valence, together with the c/a ratio and the first ionization energy are used to fit the relative oxygen site energies.

Figure 6(d) shows the result of linear fitting of the relative oxygen site energies $E_{o\text{-}t}$:

$$E_{o\text{-}t} = 5.38\ [\text{eV}] - 0.75\ [\text{eV/e}]v_{\text{eff}} + 0.0029\ [\text{eV/kJ}\cdot\text{mol}]E_{\text{ion}} - 3.31\ [\text{eV}]\frac{c}{a}, \quad (6)$$

where v_{eff} is the effective valence, E_{ion} is the first ionization energy, and the c/a ratio. From this fit with $R^2 = 0.8240$, oxygen site stability can be understood in terms of how easy it is for the oxygen interstitial to gain the extra electrons it needs from the surrounding lattice. An oxygen interstitial is further from its lattice neighbors when in the octahedral site when compared to the tetrahedral site, making it more difficult

for charge transfer to occur. However, this can be offset by the fact that the octahedral site has six lattice neighbors compared to four neighbors for the tetrahedral. As valence increases, it becomes easier for oxygen to obtain electrons from the surrounding atoms and octahedral sites become more stable relative to tetrahedral sites. This is because oxygen only wants a certain amount of charge, and thus no further reduction in tetrahedral site energy is gained after a certain point. Through Bader charge analysis [32,33] we have found that although charge transfer to the oxygen atom varies between hcp elements, within each element the oxygen charge transfer is almost the same for all interstitial sites. The same argument applies to the first ionization energy, where a decrease in the ionization energy will stabilize the octahedral relative to the tetrahedral. The c/a ratio provides a measure of how distorted the tetrahedral site is for a specific hcp lattice. A higher c/a ratio increases the distance between oxygen and one of its tetrahedral neighbors and leads to relatively more stable octahedral sites. The primary deviation for the fit is Co, which unlike all of the other hcp elements, shows magnetic ordering which provides for an additional interaction between transferred electrons.

While no general trends for oxygen diffusion extend across all 15 hcp elements in Fig. 3, much more similarities exist between elements at close proximity on the periodic table. The titanium group (Ti, Zr, and Hf) all exhibit a high barrier for oxygen transition between octahedral sites ($\sim$3 eV), and comparable activation energies for diffusion ($\sim$2 eV). Ti prefers the hexahedral site over the tetrahedral, while both Zr and Hf prefer the very similar shallow tetrahedral site. Ti and Zr are also the only two hcp elements which contain a stable nonbasal crowdion site for oxygen. In their own group, Zn and Cd both possess unusually high c/a ratios, and as a result exhibit very similar site energy differences and diffusion barriers. In the middle of the transition metals, Tc, Ru, Re, and Os all appear qualitatively the same, having relatively high T-T barriers and low O-O barriers. With the O-O barrier lower than the O-T barrier for these four elements, high diffusion anisotropy will emerge between the basal and c-axis directions. At 1000 K, $D_{c\text{ axis}}/D_{\text{basal}}$ is approximately 5 for Tc, 10 for Ru, 30 for Re, and 1000 for Os; this anisotropy grows larger at lower temperatures. In contrast, the anisotropy between c axis and basal oxygen diffusion for all other hcp systems is less than a factor of 2 over the entire temperature range. Finally, the scandium group, Sc and Y, also appear qualitatively similar in terms of their site stabilities and diffusion barriers.

IV. CONCLUSION

We have used first-principles calculation to determine oxygen diffusion pathways in 15 hcp metals as well as oxygen diffusion barriers within each element. A variety of different interstitial site combinations were discovered for oxygen in these hcp elements. Analytic diffusion equations have been derived for each unique diffusion network. Combined with calculated DFT diffusion barriers, we predict diffusivity curves for oxygen in all 15 hcp elements, which match well to available experimental data. A surprising result is the discovery that oxygen does not prefer the large octahedral interstitial site in 8 of the 15 hcp elements. Although this preference for the tetrahedral/hexahedral site is counterintuitive, it can be explained by the relative ease for oxygen charge transfer, where lower valence, higher ionization energy, and lower c/a ratio all favor the tetrahedral site more than the octahedral. The large variety of interstitial sites as well as their stability found within these 15 hcp elements should serve as a reminder that surprises can be hidden in very simple and well-studied systems.

ACKNOWLEDGMENTS

This research was supported by NSF/CMMI CAREER Award No. 0846624 and Boeing. Computational resources from the Turing and Taub clusters maintained and operated by the Computational Science and Engineering Program at the University of Illinois. This work used the Extreme Science and Engineering Discovery Environment (XSEDE) [42], which is supported by National Science Foundation Grant No. ACI-1053575 at the Texas Advanced Computing Center. The 3D models in Fig. 2 are visualized with VMD [43] and rendered with Tachyon [44].

[1] R. G. Hennig, D. R. Trinkle, J. Bouchet, S. G. Srinivasan, R. C. Albers, and J. W. Wilkins, Nat. Mater. **4**, 129 (2005).
[2] A. Borghesi, B. Pivac, A. Sassella, and A. Stella, J. Appl. Phys. **77**, 4169 (1995).
[3] J. P. Hirth, Metall. Trans. A **11**, 861 (1980).
[4] M. L. Wasz, F. R. Brotzen, R. B. McLellan, and A. J. Griffin, Int. Mater. Rev. **41**, 1 (1996).
[5] Z. Liu and G. Welsch, Metall. Mater. Trans. A **19**, 1121 (1988).
[6] V. B. Vykhodets, S. M. Klostman, T. Y. Kurennyk, A. D. Levin, and V. A. Pavlov, Phys. Met. Metallogr. **68**, 94 (1989).
[7] F. L. Bregolin, M. Behar, and F. Dyment, Appl. Phys. A **86**, 481 (2007).
[8] J. P. Pemsler, J. Electrochem. Soc. **106**, 1067 (1959).
[9] J. D. Gadd and E. B. Evans, Corrosion **17**, 441t (1961).
[10] G. R. Wallwork and W. W. Smeltzer, J. Electrochem. Soc. **110**, 943 (1963).
[11] E. Bisogni, G. Mah, and C. Wert, J. Less-Common Met. **7**, 197 (1964).
[12] F. Bernardi, M. Behar, A. Ruzzarin, J. H. R. dos Santos, and F. Dyment, Appl. Phys. A **83**, 37 (2006).
[13] I. G. Ritchie and A. Atrens, J. Nucl. Mater. **67**, 254 (1977).
[14] B. J. Flinn, C.-S. Zhang, and P. R. Norton, Phys. Rev. B **47**, 16499 (1993).
[15] G. M. Hood, H. Zou, S. Herbert, R. J. Schultz, H. Nakajima, and J. A. Jackman, J. Nucl. Mater. **210**, 1 (1994).
[16] B. Li, A. R. Allnatt, C.-S. Zhang, and P. R. Norton, Surf. Sci. **330**, 276 (1995).
[17] H. J. Borchardt, J. Inorg. Nucl. Chem. **26**, 711 (1964).

[18] O. N. Carlson, F. A. Schmidt, and D. T. Peterson, J. Less-Common Met. **10**, 1 (1966).
[19] K. Kuroda, T. Yoshida, T. Fujisawa, and C. Yamauchi, J. Mining Mater. Process. Inst. Japan (Shigen-to-Sozai) **113**, 179 (1997).
[20] F. A. Schmidt and O. N. Carlson, J. Less-Common Met. **50**, 237 (1976).
[21] H. H. Wu and D. R. Trinkle, Phys. Rev. Lett. **107**, 045504 (2011).
[22] S. C. Middleburgh and R. W. Grimes, Acta Mater. **59**, 7095 (2011).
[23] P. Zhang, J. Zhao, and B. Wen, J. Nucl. Mater. **423**, 164 (2012).
[24] A. O'Hara and A. A. Demkov, Appl. Phys. Lett. **104**, 211909 (2014).
[25] *International Tables for Crystallography*, 5th ed., Vol. A, edited by T. Hahn (Kluwer Academic, Dordrecht, 2002).
[26] G. Kresse and J. Hafner, Phys. Rev. B **47**, 558 (1993).
[27] G. Kresse and J. Hafner, Phys. Rev. B **49**, 14251 (1994).
[28] G. Kresse and J. Furthmüller, Comput. Mater. Sci. **6**, 15 (1996).
[29] G. Kresse and J. Furthmüller, Phys. Rev. B **54**, 11169 (1996).
[30] G. Kresse and D. Joubert, Phys. Rev. B **59**, 1758 (1999).
[31] J. P. Perdew, K. Burke, and M. Ernzerhof, Phys. Rev. Lett. **77**, 3865 (1996).
[32] M. Yu and D. R. Trinkle, J. Chem. Phys. **134**, 064111 (2011).
[33] D. R. Trinkle and M. Yu, BADER INTEGRATION, https://github.com/DallasTrinkle/BaderIntegration.
[34] G. Mills and H. Jónsson, Phys. Rev. Lett. **72**, 1124 (1994).
[35] G. Henkelman, B. Uberuaga, and H. Jónsson, J. Chem. Phys. **113**, 9901 (2000).
[36] D. R. Trinkle, Philos. Mag. (2016), doi:10.1080/14786435.2016.1212175.
[37] D. R. Trinkle and A. Jain, ONSAGER v1.2, doi:10.5281/zenodo.57407
[38] D. Singh and Y. P. Varshni, Phys. Rev. B **24**, 4340 (1981).
[39] C. Pantea, I. Stroe, H. Ledbetter, J. B. Betts, Y. Zhao, L. L. Daemen, H. Cynn, and A. Migliori, J. Phys. Chem. Solids **69**, 211 (2008).
[40] A. F. Guillermet and G. Grimvall, J. Less-Common Met. **147**, 195 (1989).
[41] G. H. Vineyard, J. Phys. Chem. Solids **3**, 121 (1957).
[42] J. Towns, T. Cockerill, M. Dahan, I. Foster, K. Gaither, A. Grimshaw, V. Hazlewood, S. Lathrop, D. Lifka, G. Peterson, R. Roskies, J. Scott, and N. Wilkins-Diehr, Comput. Sci. Eng. **16**, 62 (2014).
[43] W. Humphrey, A. Dalke, and K. Schulten, J. Mol. Graphics **14**, 33 (1996).
[44] J. Stone, An Efficient Library for Parallel Ray Tracing and Animation, Master's thesis, Computer Science Department, University of Missouri-Rolla, 1998.